

Contents lists available at ScienceDirect

Journal of Materials Research and Technology

journal homepage: www.elsevier.com/locate/jmrt



Check for updates

Interaction of contour and hatch parameters on vertical surface roughness in laser powder bed fusion

Tianyu Zhang, Lang Yuan

Department of Mechanical Engineering, University of South Carolina, Columbia, SC, 29201, USA

ARTICLE INFO

Handling editor: L Murr

Keywords:
Additive manufacturing
Surface roughness
Contour offset distance
Melt pool migration
Dross formation

ABSTRACT

In Laser Powder Bed Fusion (L-PBF), surface roughness is pivotal for controlling the mechanical and functional performances, as well as the geometrical accuracy of the final product. This study extensively investigated the interactions of hatch and contour processing parameters, along with contour offset distance, on vertical surface roughness for 316L stainless steel in L-PBF. Melt pool morphology and surface arithmetic average roughness (Sa) were quantified using confocal microscopy, while scanning electron microscopy was employed to interpret the detailed microstructure of surface features. Under low volumetric energy density (VED) hatch conditions (e.g., 66.7 J/mm³), varying the contour offset distance has a negatable effect on the surface roughness when the contour VED is lower than 121.6 J/mm³, remaining relatively smooth surfaces dominated by bare melt tracks with sparely attached partially melted particles. Increasing the hatch or contour VED (e.g., 166.7 J/mm³), dross formation, identified by the microstructural differences and explained by the melt pool instability and migration, is inevitable, which dictates the surface roughness with higher Sa values. The larger contour offset distance further promotes the dross occurrence with irregularity and increases Sa. Employing a low contour VED with an appropriate offset distance and adopting the contour-first scan strategy was demonstrated as an effective solution to reduce the dross formation. Through the analysis of melt pool behavior, surface topography, and microstructure, this study elucidates the mechanisms governing dominant surface characteristics under the combined influence of hatch and contour parameters. It lays the foundation for precise control of surface roughness without altering hatching parameters, enabling the tailored manipulation of performance in additively manufactured structures.

1. Introduction

Laser Powder Bed Fusion (L-PBF) presents a distinctive amalgamation of advantages, encompassing high design flexibility, tailored properties regulation, minimal geometric tolerances, and superior product integrity [1]. Consequently, it has emerged as a prevalent manufacturing technique for intricate components across industrial sectors like biomedical and aerospace [2]. The surface roughness of L-PBF-produced components not only influences the geometric precision of the product [3] but also profoundly impacts their functional and structural performances [4,5]. For instance, in heat exchangers, surface roughness can modulate the heat transfer efficiency [6,7], whereas in tubular products, it affects the liquid flow rate and permeability [8]. Surface features impact the sound absorption rate at different broadbands for acoustic applications [9]. Due to the favorable crack initiation sites provided by rough surface features [10], the surface roughness

exerts discernible effects on specific mechanical attributes, such as fatigue endurance [11]. Although post-processing methods (such as peening and electric polishing) have been employed to improve surface quality [12,13], their applications to intricate geometric products, such as inner small channels with high curvatures, remain ineffective or hard to control [14,15]. Prioritizing the as-built vertical surface quality in L-PBF, therefore, is of importance to tailor the desired performances.

Previous studies of vertical or downfacing surface roughness have mainly focused on the impact of contour processing parameters. Muhammad et al. [16] employed an artificial neural network (ANN)-based machine learning model and showed that the contour parameters mainly controlled the vertical surface roughness instead of the choice of hatch parameters for a rode geometry with AlSi10Mg. With a focus on the contour parameters, Buchenau et al. [17] concluded that the increasing contour speed results in more attached particles on the surface, leading to a coarser vertical surface finish, while the bulk

E-mail address: langyuan@cec.sc.edu (L. Yuan).

^{*} Corresponding author.

properties were not significantly impacted by varying the contour scan parameter in AlSi7Mg0.6. The related work has been conducted by Gockel et al. [18] to investigate the effect of contour processing parameters on vertical surface roughness in alloy 718 pillar samples with constant hatch parameters and contour offset distance. Their findings indicated that an increase in scanning speed led to insufficient energy input with greater melt pool instability and balling, resulting in larger notches between layers and elevated surface roughness. This observation contradicted the result from Yang et al. [19] by adjusting the energy density to modify the surface quality in Hastelloy X samples. With an increasing contour scan speed and smaller melt pool dimensions, improved surface roughness was achieved by less attached particles and melt pool protrusion at down skins. This difference was led by various melt pool morphology and instability at different energy density levels. Except for the impact of contour power and speed, Klingaa et al. [20,21] also demonstrated that the channel surface roughness and its variation decrease with increasing print orientation angle in straight channels due to the fewer sintered particles on the surface for 17-4 PH stainless steel

Besides studying processing parameters on vertical surface quality, the surface characteristics and their formation mechanism have been explored. Partially attached particles have been commonly recognized as one of the dominant surface roughness [22]. The bare melt pool flow pattern [23], spatters [24], and dross [25] have also been reported as other features observed on vertical surfaces. Feng et al. [26] illustrated that the domination of down skin surface features transmits from the powder adhesion to the adhesion of powder clusters, severe warp deformation, and dross formation as the overhang angle increases with increasing Ra (arithmetic average roughness) values. To elucidate the dross formation mechanism and its influence on the quality of downward-facing surfaces, Charles et al. [27,28] suggested that the loose powder's low thermal conductivity and inability to conduct heat away effectively result in a keyhole-like melt pool drilling into the powder bed, which forms the dross and degrades the down skin surface quality. It is noteworthy that the phenomenon of dross formation has been rarely reported in studies focusing on vertical surfaces. This study further explores the fundamentals of dross formation, including the variations of dross, mechanisms, and the associated process conditions.

Previous researchers have extensively discussed surface roughness and surface characteristics of vertical or down surfaces under different process conditions. However, the interaction between the hatch and contour parameters has not been investigated. In addition, the dominant vertical surface characteristics and their formation mechanisms have not been interpreted for a wide range of processing parameters. This study has conducted a systematic investigation to discuss the impact of the hatch and contour parameters and their combinations on the characteristics of vertical surfaces. The contour offset distance, as an essential parameter connecting contour and hatches, is also designed as an input under constant hatch and contour conditions. Microstructure analysis has been exclusively employed to explain the solidification behavior, dross's formation mechanism on vertical surfaces, and the differences between spatters and dross. Established on the observed phenomena, methods to improve the vertical surface quality are proposed to account for diverse requirements without changing the hatch processing parameters.

2. Methodology

Cubic specimens with the dimensions of 10 mm \times 10 mm \times 10 mm were fabricated using an Aconity MIDI L-PBF machine to investigate surface characteristics on the vertical surfaces. Gas-atomized 316L stainless steel powder, purchased from Carpenter Technology Corporation, was utilized, featuring a particle size distribution ranging from 15 to 45 μm , with an average particle size of 30 μm . An argon inert gas environment was maintained in the build chamber to minimize oxidation, ensuring an oxygen level below 100 ppm during the printing

process. A simple hatch scanning strategy was employed with a 90-degree rotation angle between successive layers with better observation of melt pool morphologies. Skywriting mode was implemented to mitigate the effects of laser acceleration and deceleration, thereby providing a clearer depiction of the melt pool characteristics [19].

Volume energy density (VED) is calculated by $VED = \frac{P}{S*Th*H}$ to express the input energy value of the laser, where P is laser power, S is scanning speed, H is the hatch distance, and Th is the layer thickness. Throughout the experiments, the hatch distance and laser spot size were consistently maintained at 100 µm, while the layer thickness remained fixed at 30 µm. Leveraging insights learned from our prior investigation under constant contour offset distance, it was established that high VED (166.7 J/mm³) generally yields a rough vertical surface attributed to dross formation, whereas low VED (66.7 J/mm³) results in a smooth vertical surface primarily characterized by bare melt tracks and adherent particles. Consequently, the processing parameters selected for this study were as follows: 260 W, 1300 mm/s (VED of 66.7 J/mm³), which corresponds to the lowest vertical surface Sa value (11.31 μm) with minimal defect occurrence (less than 2% porosity); and 800 W, 1600 mm/s (VED of 166.7 J/mm³), which exhibits the highest vertical surface Sa value (43.24 μm) [25]. In addition to these two conditions, an intermediate VED condition was added by averaging power and speed parameters, resulting in a combination of 530 W and 1450 mm/s (VED of 121.6 J/mm³). These three combinations of laser power and speed facilitated the fabrication of nine orthometric hatch parameters and contour parameters to systematically investigate the individual impacts of hatch and contour process parameters, as illustrated in Fig. 1 (a). All nine samples were produced with a constant contour offset distance of

Besides the hatch and contour processing parameters, the contour offset distance was further designed as part of the experiments on vertical surface quality. Commercial software, Autodesk Netfabb, was utilized for generating scan path files. Hatch scans were generated first, followed by contour scans where outer offset distances ranged from 0 to 200 μm , with a 25 μm gap beyond the geometry boundary. In this set, the contour and hatch scans utilized identical processing parameters as previously chosen, namely 260 W (1300 mm/s), 530 W (1450 mm/s), and 800 W (1600 mm/s). The explored conditions are depicted in Fig. 1 (b). Fig. 2 Illustrates contours with outer offset distances of 100 μm , 150 μm , and 200 μm . For all experimental conditions, contour scans were conducted following hatch scans. Each condition was printed three times to verify the repeatability and reliability of the results.

The samples are labeled using the convention HP*_CP*_D* to represent the process parameters for ease of reference. For example, HP260_CP800_D100 presents the hatch power of 260 W (with a speed of 1300 mm/s), the contour power of 800 W (with a speed of 1600 mm/s), and the contour offset distance of 100 μm .

The surface topography of samples was captured by Keyence VHX-5000 digital microscopy, where the height value for each location Z(x,y) was acquired. Sa, the arithmetical mean height of the surface, is employed to quantify the surface roughness, which is calculated by: $S_a = \frac{1}{M} \int_A |Z(x,y)| dxdy$, where A represents the area. For each sample, the surface topography images were taken at all four vertical surfaces, and an average of Sa was taken to minimize the error from measurements.

The samples underwent a series of preparation steps, including cutting, grinding, polishing, and etching, to assess the morphologies of melt pools and solidification microstructures at the surface boundary. The cutting plane was oriented perpendicular to the laser scanning direction of the top layer. The samples were etched with the aqua regia for 15 s. Melt pool morphologies were imaged using digital microscopy, with measurements of melt pool width and depth conducted five times to establish average values. Zeiss GeminiSEM 500 Scanning Electron Microscopy (SEM) was employed to characterize the microstructure, including subgrains, to explain the forming mechanisms of the surface features. The primary dendrite arm spacing (PDAS), indicative of

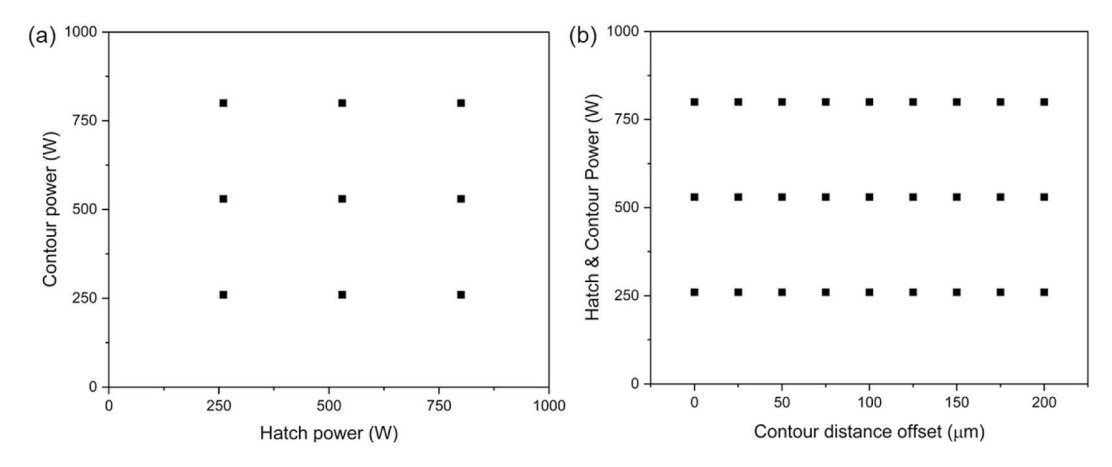


Fig. 1. Experimental conditions: (a) varying contour and hatch power and speed, (b) varying contour offset distance.

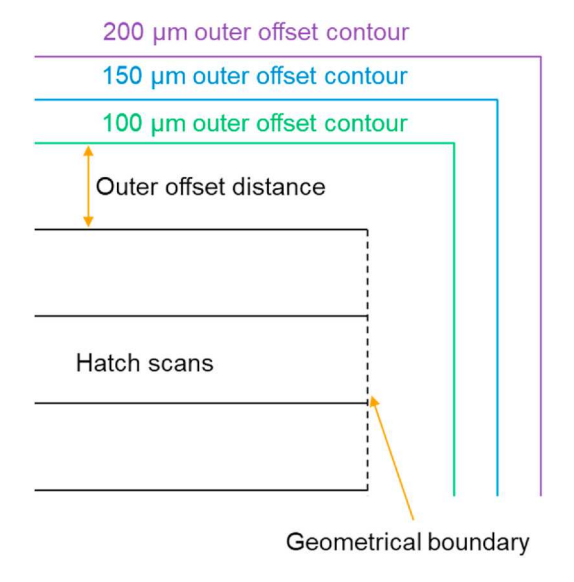


Fig. 2. Illustration of contour scans with different offset distances.

cellular subgrain microstructure, was measured using the mean linear intercept method outlined in ASTM E112 for representative samples, providing insights into solidification conditions [29].

3. Result and discussion

3.1. Melt pool morphology

The melt pool morphology serves as an indicator of melt pool instability during the printing process, with direct implications for surface characteristics. Fig. 3 illustrates the melt pool on the top surface of samples under various processing parameters, with the build direction (BD) marked for clarity. Table 1 presents the melt pool dimensions for each condition. Melt pool shape transitions from a cross-sectional ellipse shape at HP260_CP260_D100 to a half-ellipse shape at HP800_CP800_D100. The dimensions of the melt pool and the melt pool width-to-depth ratio increase with the elevated VED, as detailed in Table 1. These ratios range from 1.72 to 2.42, suggesting that melt pool fabrication predominantly occurred under the conduction mode of melting [30].

The changes in melt pool shape can be attributed to several factors, including improved wetting conditions, extended solidification time at higher melt liquid temperatures, and intensified Marangoni flow under high VED conditions [31]. As shown in Fig. 3, with increasing VED, a larger melt pool facilitates a larger connection region with previously

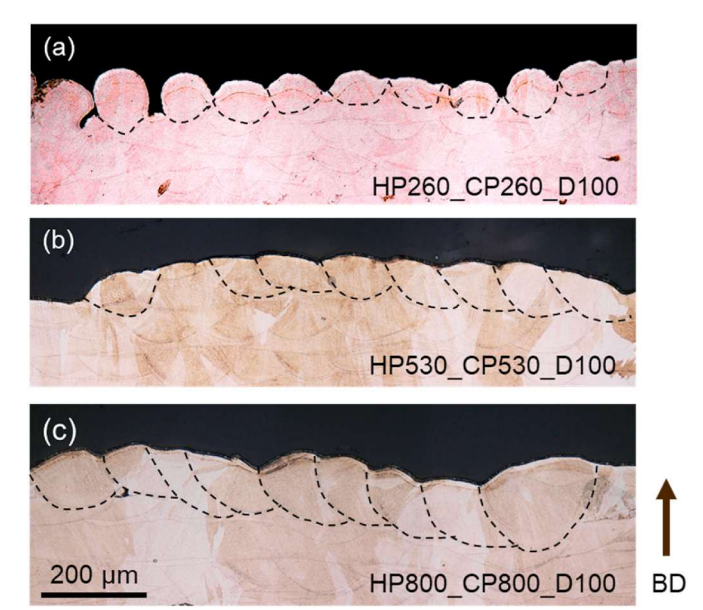


Fig. 3. The melt pool morphology under different process conditions: (a) HP260 CP260 D100, (b) HP530 CP530 D100, (c) HP800 CP800 D100.

Table 1
Melt pool dimension and width-to-depth ratio at different conditions.

Sample	Melt pool width	Melt pool depth	Width-to-depth ratio
HP260_CP260_D100	$85.3 \pm 5.9 \ \mu m$	$49.6 \pm 4.2 \mu m$	1.72
HP530_CP530_D100	$158.7\pm10.3~\mu m$	$66.99\pm8.8~\mu m$	2.36
HP800_CP800_D100	221.78 ± 25.4	91.39 ± 12.6	2.42
	μm	μm	

solidified melt tracks while reducing the contact angle of the liquid. The elevated melt pool temperature and elongated solidification time reduce liquid viscosity and provide sufficient time for gravity to flatten melt pool protrusions. Furthermore, the Marangoni force, arising from surface tension gradients, plays a critical role in driving fluid flow and consequently influencing the morphology of the melt pool [32,33]. For 316L stainless steel, the surface tension coefficient is negative when sulfur levels are at 75 ppm and oxygen levels are below 570 ppm [34, 35], indicating a centrifugal outward direction of Marangoni flow. With the increased VED input, a more pronounced Marangoni flow accelerates fluid motion, expanding its width and resulting in a shallower, wider melt pool, as depicted in Fig. 3 (c).

3.2. Characteristics of vertical surfaces

To provide a comprehensive understanding of vertical surface characteristics, the top-down topographies and cross-sectional melt pool morphologies of the selected samples are shown in Fig. 4. Note that the scale of the color bar is different to better illustrate the features on the surfaces. At HP260 CP260 D100 condition (Fig. 4 (a1) and (a2)), bare melt tracks and unmelted powders are observed on vertical surfaces with a low Sa value of 15.02 μm . On the other hand, at HP800_CP800_D100 condition, melt pools exhibit a downward trend, coalescing into a crosssectional ellipse shape, contributing to a rough vertical surface (Sa of 30.97 μ m), as shown in Fig. 4 (c2). This feature, also evident in Fig. 4 (c1), is recognized as dross [27,28]. At HP530_CP530_D100 condition (Fig. 4 (b1) and (b2)), dross is accompanied by bare melt tracks with attached powders, presenting mixed features of 260 W and 800 W conditions. These observations align with the prior research [25], indicating that at low VED conditions, bare melt tracks and attached unmelted powder predominate vertical surface roughness, while large-sized dross dominates it at high VED conditions.

3.2.1. Dross formation

The formation of dross at the vertical surfaces between the bulk material and powder has been recognized as a multilayer process, primarily driven by the migration of large melt pools [25]. In contact with the vertical surfaces, the lower effective thermal conductivity of the loose powder, compared to the solidified bulk material, leads to diminished heat transfer within the powders [36]. This disparity gives rise to the formation of an asymmetric melt pool, which expands preferentially towards the powder area. A denudation zone also emerges near the vertical surface, driven by either the absorption of adjacent powder particles into the melt pool due to oscillatory motion or by their expulsion via gas expansion [37,38]. As the denudated powder base offers even lower thermal conductivity and less physical support to the melt pool, the asymmetric melt pool elongates and migrates from its original position into the powder region under the influence of recoil pressure and gravity. Ultimately, due to surface tension, the melt pool solidifies into a spherical shape, forming dross on the vertical surfaces.

The observed downward melt pool shape in Fig. 4 (c2) aligns with

the mechanism for dross formation. The microstructural variation within the dross provides additional evidence supporting this mechanism. Fig. 5 illustrates a typical dross and the microstructure at various locations within the dross. The PDAS serves as an indicator of the cooling rate, with elevated cooling rates resulting in smaller PDAS [39]. Near the bulk region, epitaxial growth maintains a mean PDAS of 0.61 μm, as shown in Fig. 5 (b). Conversely, a significantly larger cellular size of 1.73 µm was observed near the vertical surface. This heterogeneous microstructure suggests different solidification conditions as the melt pool migrates: In the connection region, epitaxial growth and a small PDAS imply the existing contact with bulk before solidification. Near the vertical surface, the larger PDAS implies an isolated thermal environment provided by the loose powder base and denudation zone. It's worth noting the presence of attached unmelted powder at the bottom right corner of Fig. 5 (a). The homogeneous microstructure within the attached powder suggests it remained unmelted and was attached to the melt pool.

3.2.2. Spatter on the vertical surface

In addition to dross formation, the presence of spatter on the vertical surface may also influence surface quality. Spatter, resulting from the ejection of melt pool liquid, has been reported to impact surface roughness [40,41]. Although spatter and dross may share similar topography on vertical surface roughness, their formation mechanisms and microstructures differ. Fig. 6 illustrates the microstructure of a sectional view for both spatter and dross. As shown in Fig. 6 (b), subgrains are more uniformly distributed in the spatter due to the simultaneous solidification environment, and a distinct boundary line can be observed between the spatter and the bulk material [41]. In contrast, the subgrains in dross increase the feature size from the bulk region to the vertical surface region, as depicted in Fig. 6 (c). Comparatively, the average size of the subgrains in the spatter is measured at $2.84~\mu m$ compared to a maximum of 1.46 μm in dross, indicating a slower cooling rate in the spatter. The differences can be attributed to the dross being connected with the bulk region, facilitating faster heat conduction than convection through the environment surrounding the spatter.

Both the dross and spatter impact the vertical surface quality under high VED conditions, and distinguishing them in topography images can

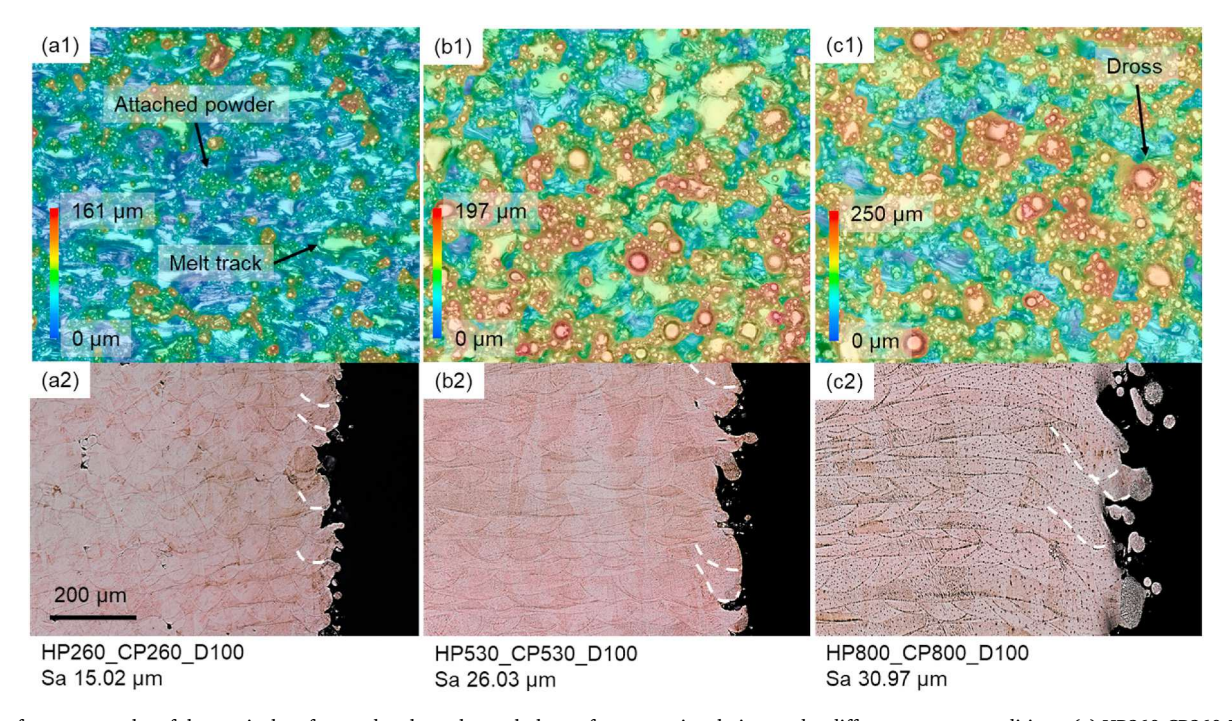


Fig. 4. Surface topography of the vertical surface and melt pool morphology of cross-sectional view under different process conditions. (a) HP260_CP260_D100, (b) HP530_CP530_D100, (c) HP800_CP800_D100.

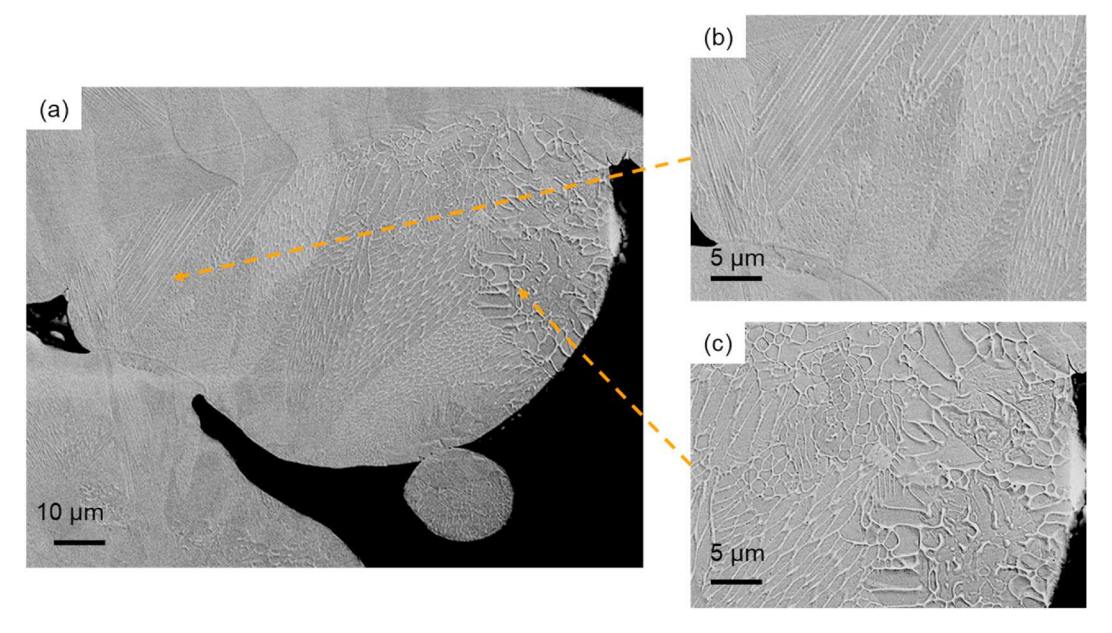


Fig. 5. Subgrain microstructure of dross at vertical surface: (a) overview of dross, (b) microstructure at the dross-bulk connection region, and (c) microstructure at the outer surface region.

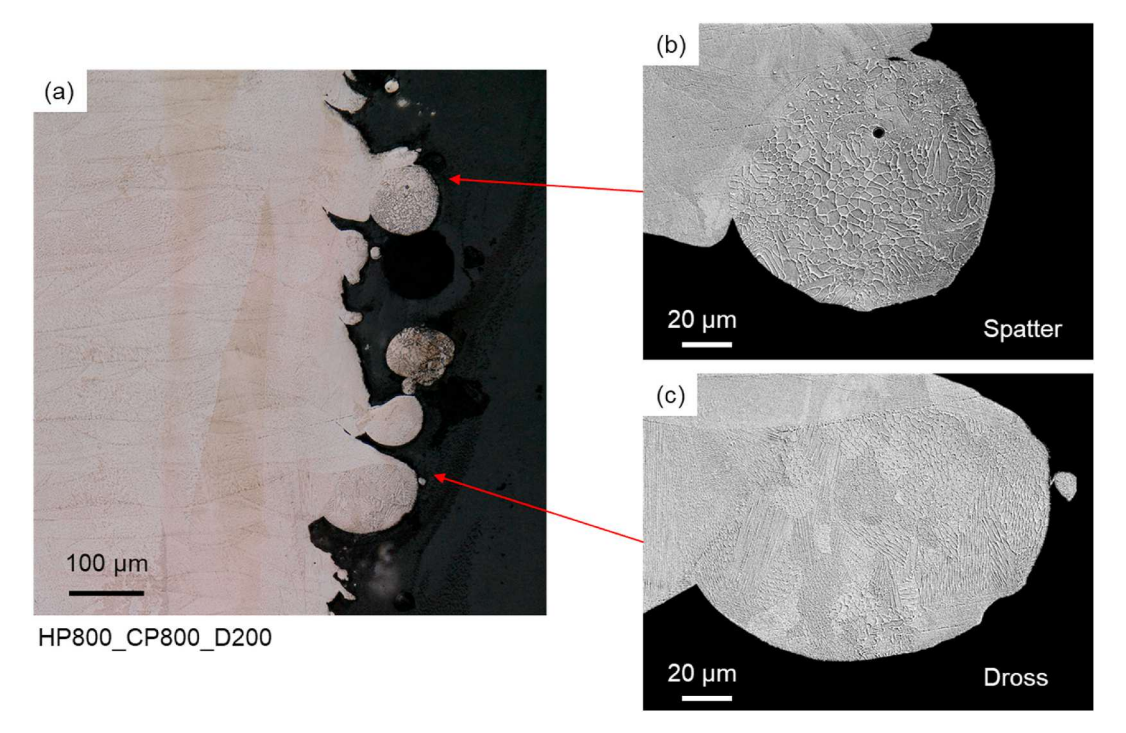


Fig. 6. Differences in dross and spatter. (a) Optical image showing both dross and spatter, (b) homogeneous distribution of microstructure in a spatter, and (c) inhomogeneous microstructure in dross.

pose a challenge. Nevertheless, the likelihood of spatter landing on the vertical surface is extremely low due to the particular location of the outer surface, leading to a rare occurrence of spatter on the vertical surface.

3.3. Surface roughness under different hatch and contour combinations

Fig. 7 illustrates the variation in Sa of vertical surfaces under the combinations of hatch and contour parameters, corresponding to the conditions listed in Fig. 1 (a). When the hatch parameter is at a high VED of 166.7 J/mm^3 (800 W and 1600 mm/s), the adjustments in contour

scan parameters exhibit minimal influence on the vertical surface Sa. The measurements yield rough surfaces, around 30 μm , for all the contour conditions. However, with reduced VEDs at 66.7 J/mm³ and 121.6 J/mm³ (260 W, 1300 mm/s and 530 W, 1450 mm/s) of the hatching parameters, an increase in contour VED correlates with elevated surface roughness. When identical contour parameters are applied, higher VEDs of the hatch parameters result in larger Sa values. Such observations suggest hatch parameters also play an essential role in vertical surface quality, differing from the conclusions made by previous studies [16,17].

To comprehensively understand the influence of hatch and contour

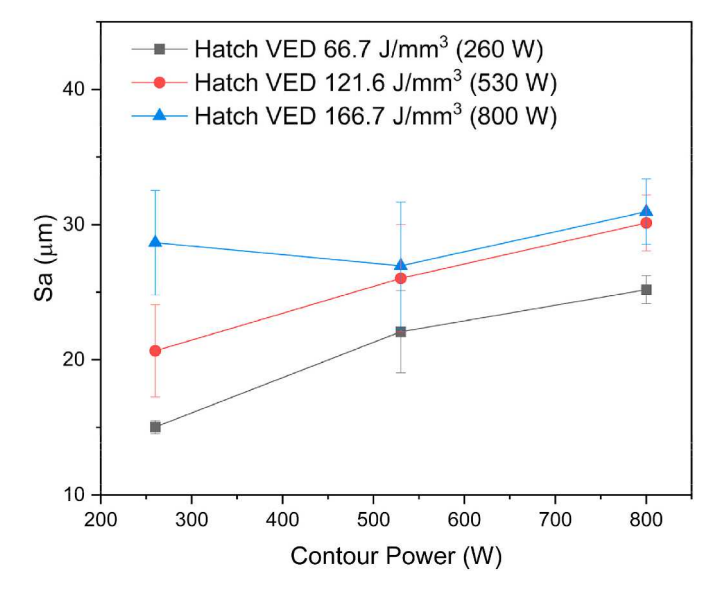


Fig. 7. Sa of vertical surfaces under different combinations of hatch and contour process conditions.

parameters on vertical surface features and roughness, top-down topographies (Fig. 8) and cross-sectional melt pool morphologies (Fig. 9) are obtained. With hatch VED of 66.7 J/mm³ (Fig. 8(a)–(d) and Fig. 9 (a)–(d)), an increase in contour VED (from 66.7 J/mm³ to 166.7 J/mm³) promotes the domination of surface features transition from bare melt tracks to dross formation, consequently deteriorating surface quality (Sa increases from 15.02 μm to 28.66 μm). In Fig. 8 (d), under the HP260_CP800_D100 condition, attached particles on the dross are not observed, and the discernible wave ripple near the boundary indicates sustained material flow during its formation stage. This phenomenon is also reflected in Fig. 9 (d), where the cross-sectional dross exhibits a cohesive integration with the bulk region, devoid of any adhered particles. Under hatch VED of 166.7 J/mm³, as shown in Fig. 8(c)-(f) and Fig. 9(c)–(f), dross at top-down topographies and the downward melt pool shapes in the cross-sectional view are observed under all conditions. In Fig. 8 (c), at HP800 CP260 D100 condition, the dross exhibits non-uniformity and rough surface texture, featuring attached particles, indicating that the dross formation primarily stems from hatch scans and subsequently undergoes remelting during the contour scan. This phenomenon can possibly be explained by the interaction between contour and high VED hatch scans under the persistence of a wide denudation zone on the vertical surface. During subsequent contour scans, the melt track encounters a combination of irregularities from the previous track, unevenly distributed powder, and the denudation zone. This combination exacerbates the instability of the contour melt track, hindering the smoothing of vertical surfaces. Subsequent contour scans, therefore, are ineffective in eliminating surface irregularities originating from the hatch scans.

The variations in dross morphologies can be observed under different contours and hatch VEDs. A smoother and spherical-shaped dross exists at low hatch but high contour VED conditions. As marked in Fig. 9 (d), the HP260_CP800_D100 sample presents a large contour melt track (approximately 200 μm width), and the cross-sectional melt pool shape maintains high curvature. Due to the limited denudation zone and tight connection between the contour melt track and the bulk region, surface tension gathers the dross (migrated melt pool) into a spherical shape. A similar spherical dross was also observed in Fig. 8 (b). On the other hand, an irregular dross correlated with a slender downward melt pool is observed at 166.7 J/mm³ hatch conditions (HP800_CP800_D100 sample), as shown in Figs. 8 (c) and 9 (c). Since the contour scans face uneven powder distribution, they remain high melt pool instability with reduced wetting at high VED hatch conditions, resulting in an irregular

shape.

The Sa values of the vertical surface with the hatch VED of 121.6 J/mm³ are located between the 66.7 and 166.7 J/mm³ groups in Fig. 7. As an example, the two conditions, HP530_CP260_D100 (Figs. 8(b) and 9 (b)) and HP530_CP800_D100 (Figs. 8(e) and 9(e)) demonstrated a combination of characteristics of 260 and 800 W hatch conditions, combining the dross and attached particles. The Sa values maintain an intermediate value of 20.67 μm and 30.12 μm , respectively.

3.4. Vertical surface Sa with contour offset distance

As the contour scans with low VEDs have shown limited impact on altering the surface roughness initiated from hatch scans with high VEDs, varying the offset distance between hatch and contour scans is exclusively explored here to understand its role on vertical surface roughness. Fig. 10 shows the Sa of vertical surfaces with contour offset distances ranging from 0 μm to 200 μm . Under relatively high VED of 121.6 J/mm³ and 166.7 J/mm³, corresponding to 530 W, 1450 mm/s and 800 W, 1600 mm/s process conditions, the Sa generally increases with the contour offset distances. However, Sa maintained a similar value of around 16 μm when increasing contour offset distances at a low VED condition of 66.7 J/mm³. Moreover, consistent with the observations in Fig. 7, the Sa values are getting larger under the identical contour offset distance when the contour and hatch parameters are with higher VEDs.

The surface topography and etched sectional view of melt pools are presented in Figs. 11 and 12 to investigate the progression of Sa values in Fig. 10. The surface features observed in the topography images align with those in the sectional views. As shown in Fig. 11(a) and (b) and Fig. 12(a) and (b), dross dominates the surface under a high VED of 166.7 J/mm³. For example, under a 75 μm contour offset, the contour melt tracks traverse the previously migrated hatch scans, leading to a Sa of 29.06 μ m, as marked in Fig. 12 (a). Under a 200 μ m contour offset, the dross protrudes further from the bulk region, resulting in a higher Sa of 38.67 µm (Figs. 11 (b) and 12 (b)). The larger contour offset exacerbates the separation between the contour melt track and the bulk material, thereby deteriorating the wetting conditions and increasing the instability of the melt pool, which further facilitates the formation of dross and rougher vertical surfaces. Comparable melt pool morphologies and surface features are observed under the VED 121.6 J/mm³ contour and hatch conditions, where an elevation in Sa is observed with increasing contour offset distance, as shown in Fig. 11(c) and (d) and Fig. 12(c) and

At low VED condition of 66.7 J/mm³ (Fig. 11(e) and (f) and Fig. 12 (e) and (f)), the predominant features on the vertical surfaces are the presence of unmelted powder and bare melt tracks, irrelevant to the offset distances. The relatively small size of the melt pool, which is contributed to by low energy input, yields limited migration of the melt pool. The contour track maintains similar wetting conditions and instability with increased contour offset distance, resulting in similar vertical surface Sa. As shown in Fig. 12 (d), at the largest contour offset distance (200 μ m) in this study, a gap is observed between the contour and hatch scans at low VED conditions due to the limited melt pool dimensions (average melt pool width 85.3 µm). Such a gap does not appear with the higher VED conditions, as shown in Fig. 12(b) and (c). Not only are the melt pool dimensions larger (an average width of 158.7 μ m at VED of 121.6 J/mm³ and an average width of 221.78 μ m at VED of 166.7 J/mm³), but the melt pool from the hatches extends more to the vertical surface, facilitating the gap filling between contour and hatch tracks.

3.5. Controlling vertical surface roughness

After analyzing the factors affecting vertical surface characteristics, it is imperative to propose efficient methods to improve or control surface roughness without varying the bulk material properties, primarily

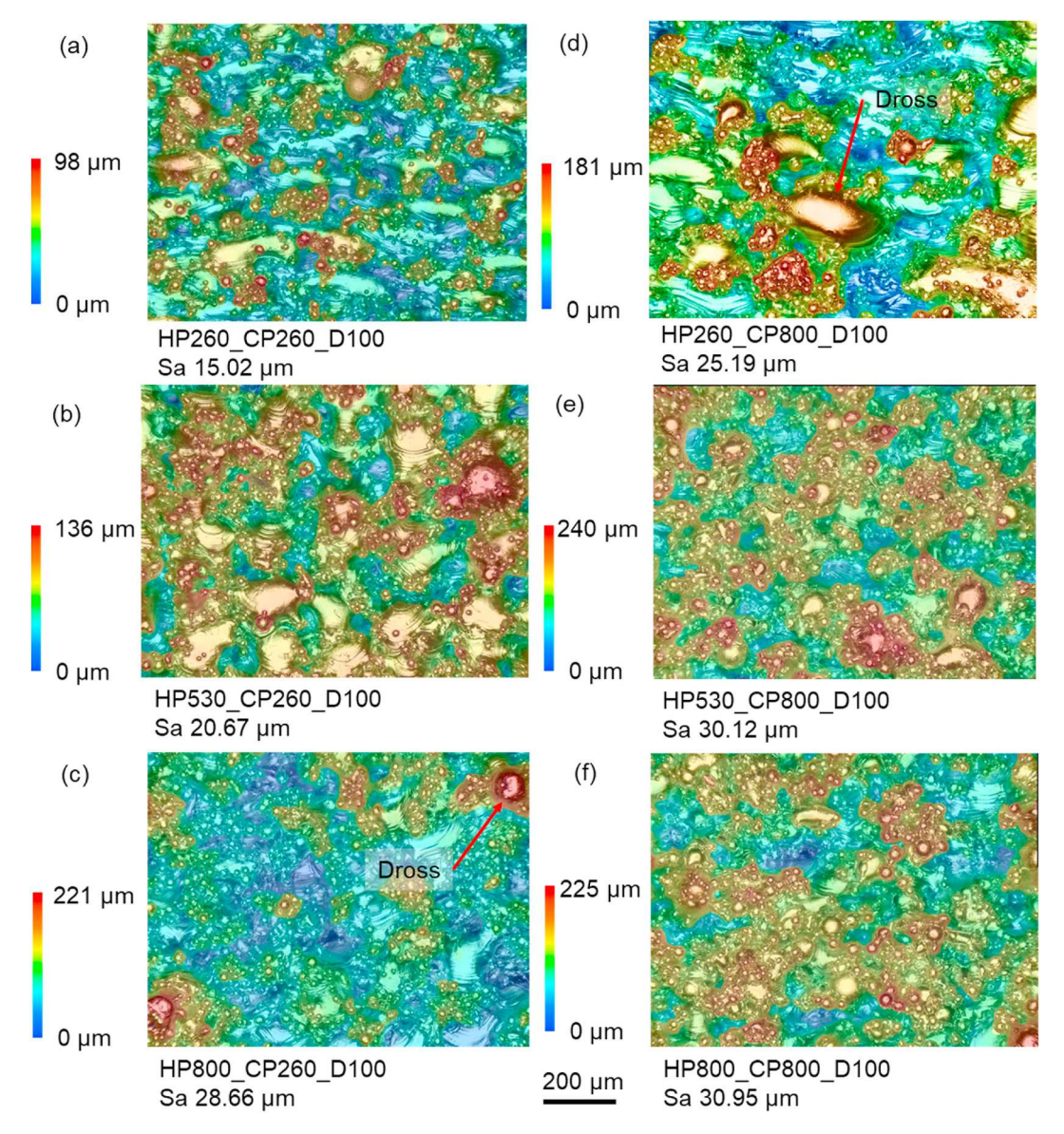


Fig. 8. Surface topography of vertical surfaces at different hatch and contour parameters.

determined by hatch parameters [17]. As explored in this study, conducting high VED contour scans results in dross formation and uneven vertical surfaces. A contour scan with low VED (e.g. 66.7 J/mm³) is necessary to achieve a smooth vertical surface. High VED hatch scans also lead to dross formation, which cannot be easily remedied by either applying a low VED contour scan with a constant offset distance or increasing the contour offset distance while maintaining the VED, as discussed. Only through applying a low VED contour with a large offset distance (e.g., 200 µm), the small melt pool fails to achieve optimal wetting conditions. It cannot address the formation of large dross, thereby exerting limited influence on vertical surface quality. Such an example is demonstrated in Fig. 13. With a 200 µm contour offset distance, the vertical surface Sa of HP800_CP260_D200 shows a similar value of 30.57 μm with HP800_CP260_D100 (28.66 μm shown in Fig. 8 (c)). Given that low VED scans result in smaller denudation zones and improved wettability for subsequent tracks, increasing the number of low VED contours (e.g., 2 or 3 contours) would progressively mitigate the adverse impact of hatch scans on vertical surface roughness. However, excessive contour scans may lead to a large dimensional error in the final product.

As this study focuses on the post-contour strategy, employing the

contour-first strategy has shown promising results in improving surface roughness [42]. It is crucial to apply a proper contour offset distance to minimize the impact of melt pool migration on the vertical surface from subsequent hatch scans. Inadequate contour offset distance (e.g., 50 µm in this study) could result in later hatch scans overwriting the contour scans due to the melt pool migration, while excessive contour offset distance can lead to gap occurrence between contour and hatch scans, thereby compromising the mechanical behavior of the final product, as depicted in Fig. 12 (f). An example of the contour-first strategy in smoothing the vertical surface was conducted, specifically denoted as HP800_CP260_D200_contourfirst, as shown in Fig. 14. Coordinated with low VED (66.7 J/mm³) contour scans at 260 W and 1300 mm/s, an improved vertical surface with a Sa value of 21.62 µm was achieved, which is comparably lower than the $28.66 \mu m$ observed in the $HP800_CP260_D100$ (Fig. 8 (c)) and the 30.57 μm in HP800_CP260_D200 (Fig. 13). Fig. 14 (a) shows that the contour scans are tightly connected to the bulk region without any prominent dross formation, while some attached powders are visible. Compared with the contour scans facing only one side of the powder in the post-contour strategy, the melt track faces both sides with powder at the contour-first scans, which increases the laser absorptivity and melt pool

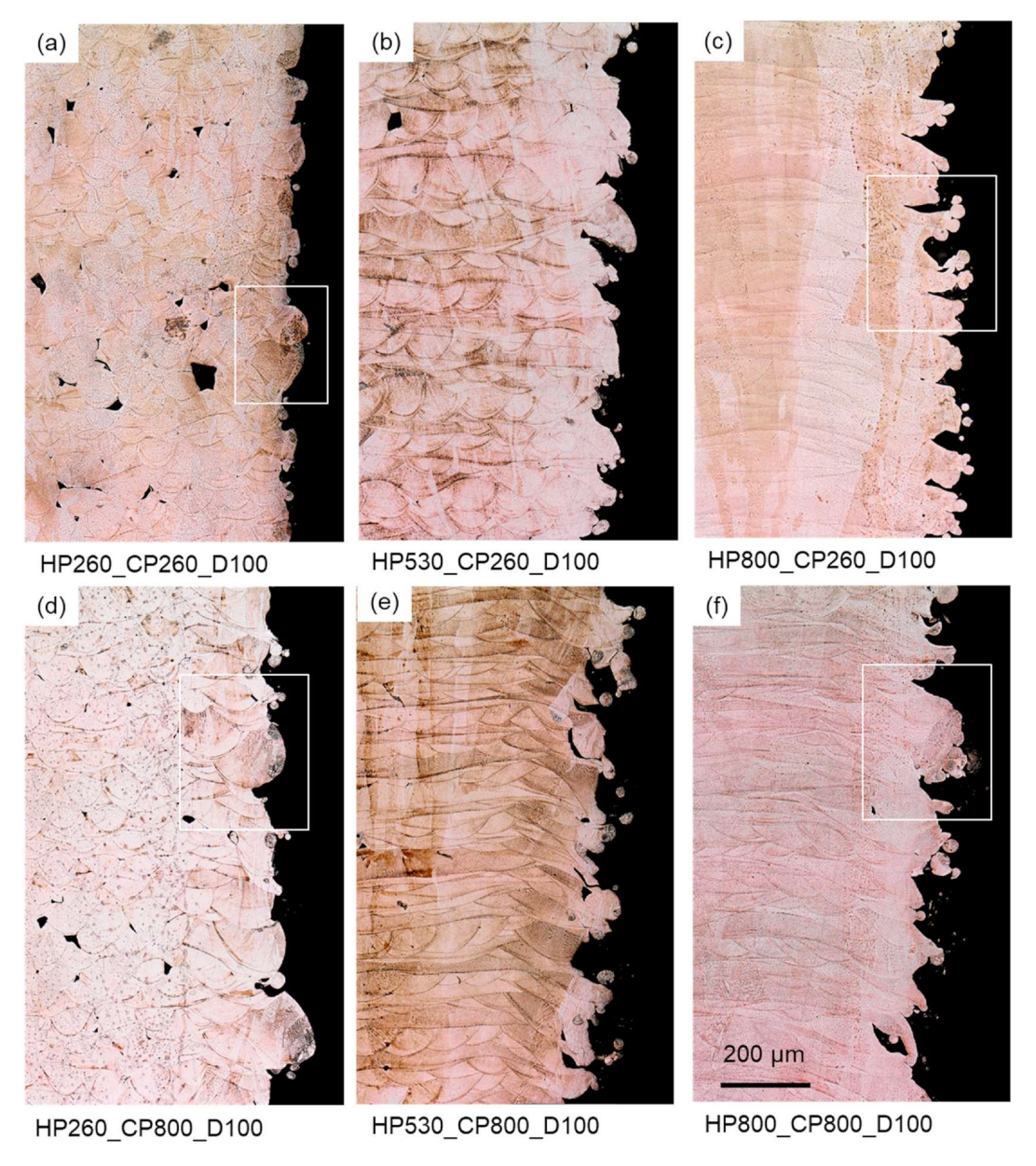


Fig. 9. Melt pool morphology on vertical surfaces.

dimensions but also results in a symmetric melt pool [42]. The appropriate contour offset distance prevents the overwriting from the high VED hatches migration, thereby inhibiting the formation of prominent dross. Although attached powders and some dross are still present on the vertical surface in Fig. 14 (b), the height of the dross has been significantly reduced from approximately 200 μm observed in HP800_CP260_D100 and HP800_CP260_D200 (as shown in Figs. 8 (c) and Fig. 13) to around 100 μm .

4. Conclusions

The interactions of contour and hatch parameters, as well as contour offset distance, on vertical surface quality, are thoroughly investigated in this study. The formation mechanisms of various surface features, including dross, spatter, bare melt tracks, and attached powder, under

different VED conditions, are analyzed through the melt pool morphology and microstructures. Based on the driving mechanisms for surface characteristics, methods for suppressing dross formation and controlling vertical surface quality are proposed.

Both the hatch and contour scans impact the vertical surface roughness. Under low VED hatch and contour conditions, the smooth vertical surfaces, quantified by low Sa values, are achieved with the domination of attached particles and bare melt tracks. With a higher contour VED, the larger melt pool results in the tendency of melt pool migration at the vertical surface boundary region, leading to dross formation and higher vertical surface roughness. With the higher hatch VED, the severer hatch melt pool migration and larger denudation left from hatch scans elevate the instability of subsequent contour tracks, consequently forming the irregular-shaped dross and rougher vertical surface.

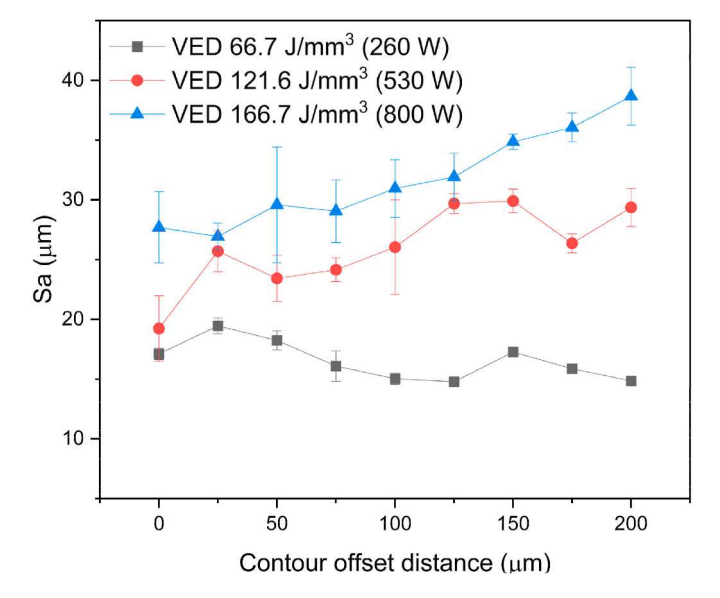


Fig. 10. Sa of vertical surfaces under different contour offset distances.

The contour offset distance shows different impacts on vertical surface roughness under different contour and hatch VEDs. Under hatch and contour parameters with low VED (e.g., $66.7 \, \mathrm{J/mm^3}$), the restricted melt pool migration and small melt pool size yield a smooth vertical surface, irrespective of the contour offset distance. However, at higher hatch and contour VED values (exceeding $121.6 \, \mathrm{J/mm^3}$), increasing the contour offset distance increases instability in the contour melt track and results in a rougher vertical surface. The Sa under higher hatch and contour VEDs consistently exceeds that at low VEDs, regardless of contour offset distance.

Overall, hatch and contour parameters with low VEDs are typically preferred to achieve a smooth vertical surface. Any dross generated by high VED hatch scans poses challenges for subsequent contour scans to remove. When hatch parameters with high VEDs are necessary, multiple contour scans with low VED or the contour-first strategy with an appropriate offset distance can mitigate the dross formation and improve the surface quality.

This study offers insights into the mechanisms that drive the surface characteristics and has demonstrated methods to improve surface quality via mitigating dross formation. By promoting a deeper understanding of the interactions between contour and hatch parameters, the research uncovers that the selection of the contour parameters for desired surface roughness is dependent on the hatch parameters. Such a

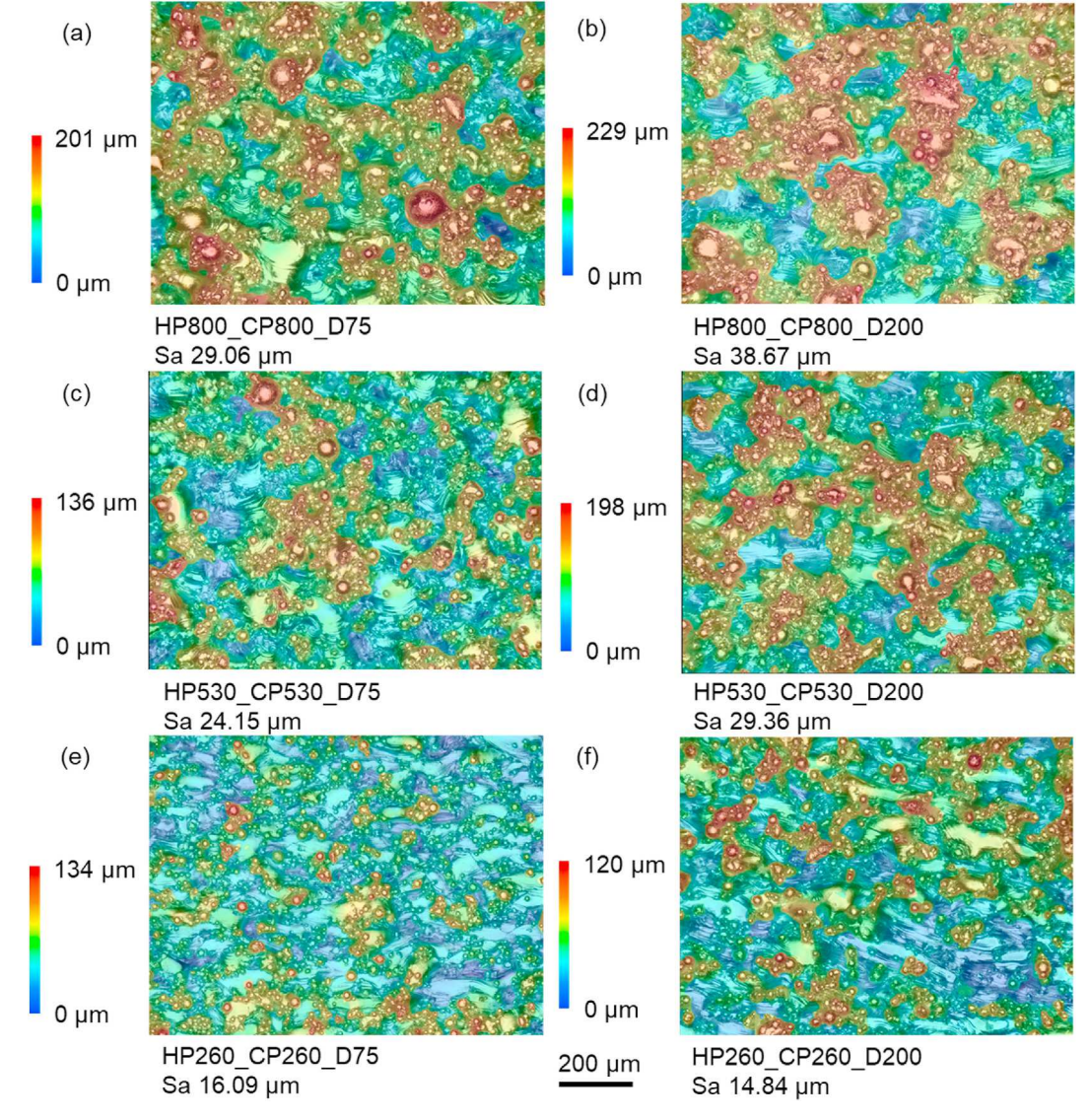


Fig. 11. Surface topography of samples with different contour offset distances.

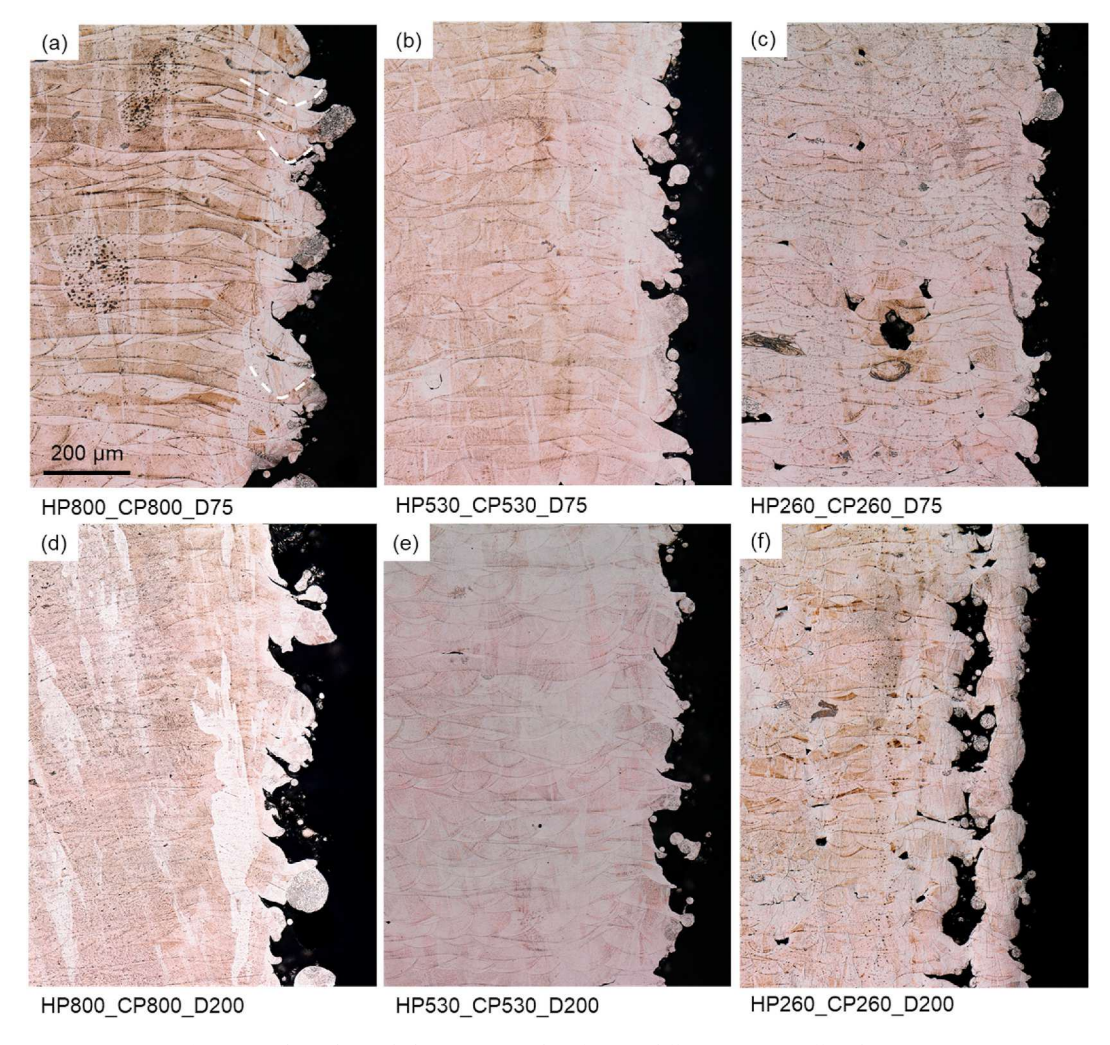


Fig. 12. Melt pool morphology on vertical surfaces at different contour offset distances.

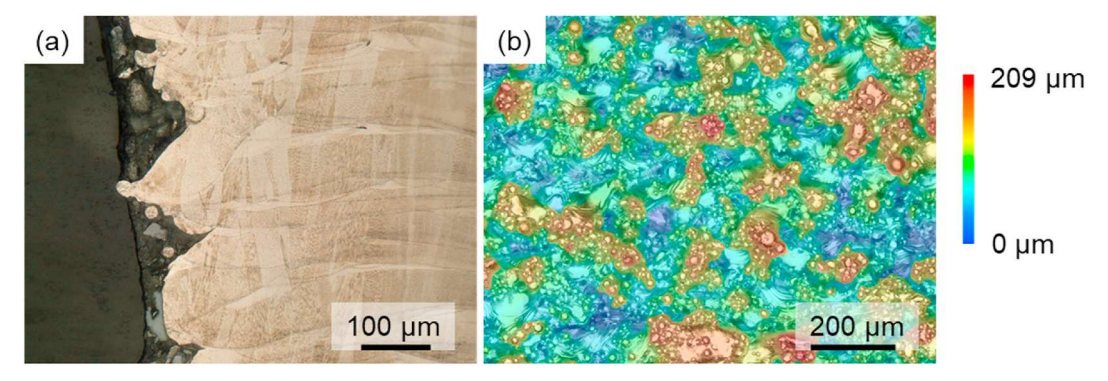


Fig. 13. (a) Melt pool morphology and (b) surface topography on the vertical surface of HP800_CP260_D200.

finding challenges the common practice of independently assigning contour parameters without considering hatch parameters. Given that the microstructure, defects, and thus, the material properties in bulk are determined by hatch parameters, the means to determining optimal contour parameters suggested in this study is expected to enhance

further geometric precision as well as the functional or structural performances of additively printed structures, particularly those with complex internal features. Although various surface post-treatment technologies, such as machining, abrasive polishing, shot peening, chemical etching, etc., have been developed for improving the surface

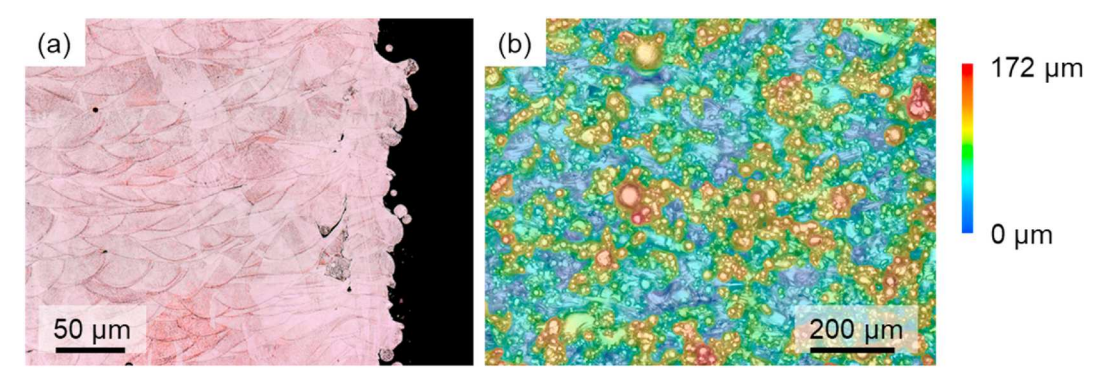


Fig. 14. (a) Melt pool morphology and (b) surface topography on the vertical surface of HP800_CP260_D200_contourfirst.

quality of additively manufactured, controlling the as-built surface quality, including roughness and features, can significantly reduce processing time and costs [15]. By linking hatch parameters with contour parameters and establishing correlations between surface characteristics and process parameters, this study offers the potential for real-time, localized control of the printing process to tailor surface roughness, thereby achieving location-dependent properties.

Nomenclature

BD	Build direction
CP	Contour power
D	Contour offset distance
H	Hatch spacing
HP	Hatch power
L-PBF	Laser powder bed fusion
P	Power
PDAS	Primary dendrite arm spacing
S	Scanning speed
Sa	Surface arithmetic average roughness
VED	Volumetric energy density

Declaration of competing interest

The authors declare the following financial interests/personal relationships which may be considered as potential competing interests: Lang Yuan reports financial support was provided by National Science Foundation. Lang Yuan reports financial support was provided by National Institute of Standards and Technology. Lang Yuan reports financial support was provided by Savannah River National Laboratory. If there are other authors, they declare that they have no known competing financial interests or personal relationships that could have appeared to influence the work reported in this paper.

Acknowledgments

The authors would like to acknowledge the support from the National Science Foundation under grant number 2029425, the U.S. Department of Commerce, the National Institute of Standards and Technology under grant number 70NANB23H030, and the U.S. Department of Energy, Savannah River National Laboratory under Contract No. 89303321CEM000080.

References

- [1] Chowdhury S, Yadaiah N, Prakash C, Ramakrishna S, Dixit S, Gupta LR, et al. Laser powder bed fusion: a state-of-the-art review of the technology, materials, properties & defects, and numerical modelling. J Mater Res Technol 2022;20: 2109–72. https://doi.org/10.1016/j.jmrt.2022.07.121.
- [2] Abd-Elaziem W, Elkatatny S, Abd-Elaziem AE, Khedr M, Abd El-Baky MA, Hassan MA, et al. On the current research progress of metallic materials fabricated

- by laser powder bed fusion process: a review. J Mater Res Technol 2022;20: 681-707. https://doi.org/10.1016/j.jmrt.2022.07.085.
- [3] Wahab Hashmi A, Ahmad S, Gulam Mustafa M, Tian Y, Iqbal F, Singh Mali H, et al. Abrasive flow finishing of 3D-Printed Aerofoils: design, numerical Simulation, and experimental analysis. Opt Laser Technol 2024;174:110578. https://doi.org/ 10.1016/j.optlastec.2024.110578.
- [4] Bhatt A, Huang Y, Leung CLA, Soundarapandiyan G, Marussi S, Shah S, et al. In situ characterisation of surface roughness and its amplification during multilayer single-track laser powder bed fusion additive manufacturing. Addit Manuf 2023; 77:103809. https://doi.org/10.1016/j.addma.2023.103809.
- [5] DelRio FW, Khan RM, Heiden MJ, Kotula PG, Renner PA, Karasz EK, et al. Porosity, roughness, and passive film morphology influence the corrosion behavior of 316L stainless steel manufactured by laser powder bed fusion. J Manuf Process 2023; 102:654–62. https://doi.org/10.1016/j.jmapro.2023.07.062.
- [6] Rastan H, Abdi A, Hamawandi B, Ignatowicz M, Meyer JP, Palm B. Heat transfer study of enhanced additively manufactured minichannel heat exchangers. Int J Heat Mass Tran 2020;161. https://doi.org/10.1016/j. ijheatmasstransfer.2020.120271.
- [7] Thompson SM, Aspin ZS, Shamsaei N, Elwany A, Bian L. Additive manufacturing of heat exchangers: a case study on a multi-layered Ti-6Al-4V oscillating heat pipe. Addit Manuf 2015;8:163–74. https://doi.org/10.1016/j.addma.2015.09.003.
- [8] Zhang J, Wang H. Magnetically driven internal finishing of AISI 316L stainless steel tubes generated by laser powder bed fusion. J Manuf Process 2022;76:155–66. https://doi.org/10.1016/j.jmapro.2022.02.009.
- [9] Zhang M, Liu C, Deng M, Li Y, Li J, Wang D. Graded minimal surface structures with high specific strength for broadband sound absorption produced by laser powder bed fusion. Coatings 2023;13. https://doi.org/10.3390/
- [10] Maleki E, Bagherifard S, Guagliano M. Correlation of residual stress, hardness and surface roughness with crack initiation and fatigue strength of surface treated additive manufactured AlSi10Mg: experimental and machine learning approaches. J Mater Res Technol 2023;24:3265–83. https://doi.org/10.1016/j. imt 2023.03.193
- [11] Raja A, Cheethirala SR, Gupta P, Vasa NJ, Jayaganthan R. A review on the fatigue behaviour of AlSi10Mg alloy fabricated using laser powder bed fusion technique. J Mater Res Technol 2022;17:1013–29. https://doi.org/10.1016/j. jmrt.2022.01.028.
- [12] Anand Kumar S, Anigani SR, Mathias S, Shrivastava A, Raghupatruni P. Effect of duplex post-processing treatment on the surface texture characteristics of AlSi10Mg alloy processed by laser powder bed fusion technique. Jom 2023;75: 1672–83. https://doi.org/10.1007/s11837-023-05770-1.
- [13] Gu J, Wang X, Gao Y, Chen Y, Zhang Z, Wen J, et al. Effect of surface modification on the high temperature low cycle fatigue performance of LPBF 316L austenitic steel. Eng Fract Mech 2024;302:110094. https://doi.org/10.1016/j. engfergress.2024.110094.
- [14] Khan HM, Karabulut Y, Kitay O, Kaynak Y, Jawahir IS. Influence of the post-processing operations on surface integrity of metal components produced by laser powder bed fusion additive manufacturing: a review. Mach Sci Technol 2020;25: 118–76. https://doi.org/10.1080/10910344.2020.1855649.
- [15] Maleki E, Bagherifard S, Bandini M, Guagliano M. Surface post-treatments for metal additive manufacturing: progress, challenges, and opportunities. Addit Manuf 2021;37:101619. https://doi.org/10.1016/J.ADDMA.2020.101619.
- [16] Muhammad W, Kang J, Ibragimova O, Inal K. Experimental investigation and development of a deep learning framework to predict process-induced surface roughness in additively manufactured aluminum alloys. Weld World 2023;67: 897–921. https://doi.org/10.1007/s40194-022-01445-8.
- [17] Buchenau T, Amkreutz M, Bruening H, Mayer B. Influence of contour scan variation on surface, bulk and mechanical properties of LPBF-processed AlSi7Mg0.6. Materials 2023;16:1–17. https://doi.org/10.3390/ma16083169.
- [18] Gockel J, Sheridan L, Koerper B, Whip B. The influence of additive manufacturing processing parameters on surface roughness and fatigue life. Int J Fatig 2019;124: 380–8. https://doi.org/10.1016/j.ijfatigue.2019.03.025.
- [19] Tian Y, Tomus D, Rometsch P, Wu X. Influences of processing parameters on surface roughness of Hastelloy X produced by selective laser melting. Addit Manuf 2017;13:103–12. https://doi.org/10.1016/j.addma.2016.10.010.

- [20] Klingaa CG, Dahmen T, Baier S, Mohanty S, Hattel JH. X-ray CT and image analysis methodology for local roughness characterization in cooling channels made by metal additive manufacturing. Addit Manuf 2020;32:101032. https://doi.org/ 10.1016/j.addma.2019.101032.
- [21] Klingaa G, Dahmen T, Baier-Stegmaier S, Mohanty S, Hattel JH. Investigation of the roughness variation along the length of LPBF manufactured straight channels. Nondestr Test Eval 2020;35:304–14. https://doi.org/10.1080/ 10589759.2020.1785445.
- [22] Moura de Souza Soares F, Barbosa DM, Reis Corado HP, de Carvalho Santana AI, Elias CN. Surface morphology, roughness, and corrosion resistance of dental implants produced by additive manufacturing. J Mater Res Technol 2022;21: 3844–55. https://doi.org/10.1016/J.JMRT.2022.10.114.
- [23] Elambasseril J, Rogers J, Wallbrink C, Munk D, Leary M, Qian M. Laser powder bed fusion additive manufacturing (LPBF-AM): the influence of design features and LPBF variables on surface topography and effect on fatigue properties. Crit Rev Solid State Mater Sci 2023;48:132–68. https://doi.org/10.1080/ 10408436.2022.2041396.
- [24] Ali U, Esmaeilizadeh R, Ahmed F, Sarker D, Muhammad W, Keshavarzkermani A, et al. Identification and characterization of spatter particles and their effect on surface roughness, density and mechanical response of 17-4 PH stainless steel laser powder-bed fusion parts. Mater Sci Eng, A 2019;756:98–107. https://doi.org/10.1016/j.msea.2019.04.026.
- [25] Zhang T, Yuan L. Understanding surface roughness on vertical surfaces of 316 L stainless steel in laser powder bed fusion additive manufacturing. Powder Technol 2022;411:117957. https://doi.org/10.1016/J.POWTEC.2022.117957.
- [26] Feng S, Kamat AM, Sabooni S, Pei Y. Experimental and numerical investigation of the origin of surface roughness in laser powder bed fused overhang regions. Virtual Phys Prototyp 2021;16:S66–84. https://doi.org/10.1080/ 17452759.2021.1896970.
- [27] Charles A, Elkaseer A, Paggi U, Thijs L, Hagenmeyer V, Scholz S. Down-facing surfaces in laser powder bed fusion of Ti6Al4V: effect of dross formation on dimensional accuracy and surface texture. Addit Manuf 2021;46. https://doi.org/ 10.1016/j.addma.2021.102148.
- [28] Charles A, Bayat M, Elkaseer A, Thijs L, Hattel JH, Scholz S. Elucidation of dross formation in laser powder bed fusion at down-facing surfaces: phenomenonoriented multiphysics simulation and experimental validation. Addit Manuf 2022; 50. https://doi.org/10.1016/j.addma.2021.102551.
- [29] Sabau AS, Yuan L, Raghavan N, Bement M, Simunovic S, Turner JA, et al. Fluid dynamics effects on microstructure prediction in single-laser tracks for additive manufacturing of IN625. Metall Mater Trans B 2020:1–19. https://doi.org/ 10.1007/s11663-020-01808-w.

- [30] King WE, Barth HD, Castillo VM, Gallegos GF, Gibbs JW, Hahn DE, et al. Observation of keyhole-mode laser melting in laser powder-bed fusion additive manufacturing. J Mater Process Technol 2014;214:2915–25. https://doi.org/ 10.1016/j.jmatprotec.2014.06.005.
- [31] Zhang T, Yuan L. Melt Pool characteristics on surface roughness and printability of 316L stainless steel in laser powder bed fusion. Rapid Prototyp J 2024. https://doi. org/10.1108/RPJ-02-2024-0078. ahead-of-p.
- [32] Le TN, Lo YL. Effects of sulfur concentration and Marangoni convection on meltpool formation in transition mode of selective laser melting process. Mater Des 2019;179:107866. https://doi.org/10.1016/j.matdes.2019.107866.
- [33] Yin H, Emi T. Marangoni flow at the gas/melt interface of steel. Metall Mater Trans B 2003;34:483–93. https://doi.org/10.1007/s11663-003-0015-z.
- [34] Leung CLA, Marussi S, Towrie M, Atwood RC, Withers PJ, Lee PD. The effect of powder oxidation on defect formation in laser additive manufacturing. Acta Mater 2019;166:294–305. https://doi.org/10.1016/j.actamat.2018.12.027.
- [35] Mills KC, Keene BJ. Factors affecting variable weld penetration. Int Mater Rev 1990;35:185–216. https://doi.org/10.1179/095066090790323966.
- [36] Jamshidinia M, Kong F, Kovacevic R. Numerical modeling of heat distribution in the electron beam melting® of Ti-6Al-4V. J Manuf Sci Eng 2013;135:1–14. https://doi.org/10.1115/1.4025746.
- [37] Chen H, Yan W. Spattering and denudation in laser powder bed fusion process: multiphase flow modelling. Acta Mater 2020;196:154–67. https://doi.org/ 10.1016/j.actamat.2020.06.033.
- [38] Lei T, Rong Y, Xu J, Huang Y. Experiment study and regression analysis of molten pool in laser welding. Opt Laser Technol 2018;108:534–41. https://doi.org/ 10.1016/j.optlastec.2018.07.053.
- [39] Yuan L, Sabau AS, Stjohn D, Prasad A, Lee PD. Columnar-to-equiaxed transition in a laser scan for metal additive manufacturing. In: IOP conf ser mater Sci Eng, vol. 861. Institute of Physics Publishing; 2020. https://doi.org/10.1088/1757-899X/ 861/1/012007.
- [40] Mumtaz KA, Hopkinson N. Selective Laser Melting of thin wall parts using pulse shaping. J Mater Process Technol 2010;210:279–87. https://doi.org/10.1016/j. imatprotec.2009.09.011.
- [41] Nasab MH, Gastaldi D, Lecis NF, Vedani M. On morphological surface features of the parts printed by selective laser melting (SLM). Addit Manuf 2018;24:373–7. https://doi.org/10.1016/J.ADDMA.2018.10.011.
- [42] Ren Z, Wei D, Wang S, Zhang DZ, Mao S. On the role of pre- and post-contour scanning in laser powder bed fusion: thermal-fluid dynamics and laser reflections. Int J Mech Sci 2022;226:107389. https://doi.org/10.1016/j. ijmecsci.2022.107389.